University of Tehran

Earth Observation and Geomatics Engineering

Online ISSN: 2588-4360

Homepage: https://eoge.ut.ac.ir/

Advanced Deep Learning Methods for Converting Single-Polarized SAR Images to Fully Polarized Representations and Corresponding Freeman-Durden and H/α Feature Decompositions

Mohaddeseh Mesvari[1] , **Jalal Amini**[1]✉

1. School of Surveying and Geospatial Engineering, College of Engineering, University of Tehran, Tehran. E-mail: m.mesvari@ut.ac.ir, jamini@ut.ac.ir (Corresponding author)

Article Info

Article type:
Research Article

Article history:
Received 2024-02-15
Received in revised form 2024-08-28
Accepted 2024-10-27
Available online 2025-01-01

Keywords:
Reconstruction of fully polarized images, Radar Image Colorization, Deep Learning, U-Net++, Freeman-Durden and H/α decomposition.

ABSTRACT

Fully polarized images are renowned for their superior ability to classify land surface features compared to single-polarized images. Despite their advantages, the acquisition of fully polarized images poses significant challenges due to technical and logistical limitations. This scarcity makes it difficult to access such images or to utilize the results from decomposition algorithms like Freeman-Durden and H/α, which are specifically designed for fully polarized data. This study utilizes the UNet++ deep learning model to reconstruct fully polarized images and decomposition features, such as H/α and Freeman-Durden decompositions. The performance of this approach is evaluated using metrics such as Mean Absolute Error (MAE), Mean Squared Error (MSE), and the Universal Image Quality Index (UIQI). The results show that the deep learning models perform exceptionally well in the image reconstruction tasks. Specifically, the MAE values for the reconstructed images are below 0.1 for all methods, indicating high accuracy. The MSE values are generally below 0.025, further confirming the precision of the models. Notably, the UIQI values for the reconstruction of fully polarized images are impressive, reaching 95.95%, which highlights the excellent visual similarity between the reconstructed and original images. These findings underscore the potential of deep learning models to address the limitations associated with the availability of fully polarized images, providing a robust solution for improved environmental and land cover monitoring.

Cite this article: Mesvari, M., & Amini, J. (2023). Advanced deep learning methods for converting single-polarized SAR images to fully polarized representations and corresponding Freeman-Durden and H/α feature decompositions. *Earth Observation and Geomatics Engineering*, Volume 7, Issue 2, Pages 44-55. http//doi.org/10.22059/eoge.2024.372687.1147

Publisher: University of Tehran.

DOI: http//doi.org/10.22059/eoge.2024.372687.1147

1. Introduction

Synthetic Aperture Radar (SAR) (Chan & Koo, 2008) technology encompasses diverse elements, including polarization and classification features. SAR images are classified into various polarization types, such as Single Polarization (Single-Pol), Dual Polarization (Dual-Pol), and Full Polarization (Full-Pol or Quad-Pol), each offering unique advantages for information extraction and classification. Polarimetric SAR enhances insights into terrain and target characteristics comprehensively (Shirvany, Chabert, & Tourneret, 2012). A comparative study on SAR image classification features investigates both image and physical domains. It evaluates single-polarized and quad-pol SAR data, providing valuable insights for land use/land cover classification.

Furthermore, SAR applications in earth observation underscore the interaction of different polarization types with objects. This emphasizes the crucial role of polarization in SAR technology (Zhang, Wang, Xu, & Jin, 2017; Y. Zhou, Wang, Xu, & Jin, 2016). Understanding SAR's polarization capabilities is vital for applications like SAR image colorization and is integral to earth observation practices.

Full-polarization SAR captures data in all four polarization states (HH, VV, HV, VH), generating a more comprehensive dataset compared to single or dual polarization. This wealth of information enhances the ability to discern and interpret features within the scene. Full polarization enhances target detection, particularly in challenging environments. The combination of different polarizations helps address issues like shadowing, leading to better identification of subtle features. This makes full-polarization SAR valuable for applications such as ship detection. This kind of data minimizes interpretation ambiguity by providing a more complete picture of the scattering behavior in the observed scene. This reduction in uncertainties enhances the reliability of information extracted from SAR imagery.

The reconstruction of fully polarimetric Synthetic Aperture Radar (SAR) images from single-polarization grayscale SAR images enriches the information by transforming single-polarization grayscale SAR images into fully polarimetric ones. This process contributes to a more thorough understanding of the scene. Reconstructed fully polarimetric Synthetic Aperture Radar (SAR) images exhibit a close alignment with authentic full-pol images, ensuring not only visual similarity but also heightened data accuracy. This alignment significantly enhances the interpretation and analysis of images, leading to improved insights. Integrating deep neural networks into the reconstruction process enhances the efficient mapping of spatial features. This, in turn, enables a more precise transformation from single-pol to fully polarimetric images, harnessing the capabilities of deep learning.

Optical image colorization is divided into two primary categories: semi-automatic and fully automatic colorization. In Semi-automatic Colorization category, users actively participate in the colorization process, providing input like selecting specific areas or offering color hints (Levin, Lischinski, & Weiss, 2004). This method offers greater user control and customization, making it ideal for situations where human input is crucial. In contrast to semi-automatic methods, fully automatic colorization operates without user intervention. Advanced algorithms, often leveraging deep learning techniques, analyze grayscale images and autonomously generate colorized versions. This automated approach is well-suited for scenarios where user input is minimal or unnecessary. Convolutional Neural Networks (CNN) play a pivotal role in the fully automated colorization of Synthetic Aperture Radar (SAR) images (Oveis, Giusti, Ghio, Martorella, & Magazine, 2021). The process involves converting single-polarization SAR images into fully polarimetric representations. CNNs excel in extracting features, identifying significant patterns and structures in SAR images. This proficiency aids in comprehending the inherent characteristics of the images, contributing to precise colorization. Fully automatic colorization utilizes deep learning techniques, where CNNs analyze and learn intricate relationships within grayscale SAR images. This empowers the network to autonomously generate colorized versions without requiring user intervention. CNN architectures enhance the classification of SAR images, ensuring accurate color assignment based on learned patterns. This guarantees that the colorization process aligns with the content and features present in the SAR data. Beyond colorization, CNNs may also contribute to other aspects of SAR image processing, such as despeckling, thereby enhancing the overall image quality before the colorization stage.

In this study, we utilize the UNet++ deep learning network to map single-polarized images to fully polarized ones. Initially, feature extraction from the single-polarized images is carried out using a convolutional network. Subsequently, the mapping process to fully polarized images is executed through the convolutional layers of the UNet++ model. Notably, the training of the EfficientNet-B7 pre-trained convolutional neural network involves a pair of Synthetic Aperture Radar (SAR) images. The single-polarized image serves as the input data, while the fully polarized image acts as the target image. This methodology is implemented using the NASA/JPL UAVSAR (Q. Song, F. Xu, & Y.-Q. Jin, 2017) L-band SAR image as a reference. Additionally, besides the process of mapping single-polarized images to fully polarized ones, we have established a model to map the single-polarized images to the outcomes obtained from PolSAR target decomposition methods like Freeman-Durden and Cloude and Pottier.

While this study focuses on demonstrating the conversion from single-pol to full-pol data and the specific decomposition features, the framework is adaptable for converting various non-full-pol data forms, encompassing compact-pol and dual-pol to full-pol data or another decomposition features. The adaptability of this method

paves the way for creating a wide range of applications beyond the demonstrated conversion from single-pol to full-pol.

This article begins with a review of existing concepts and studies in the field. The next section examines the theoretical foundations and study methodology. Following that, the research results are analysed. The article concludes with a general summary in the final section.

2. Materials and Methods

In this study, we address the significance and diverse applications of fully polarized images in remote sensing across various fields. However, acquiring such images presents challenges in different geographical areas. To overcome this, we utilize Deep Learning networks to convert single-polarized VV images into fully polarized ones. Specifically, we employ the UNet++ deep learning model for this conversion process, as outlined in the preceding section. Additionally, we highlight the pivotal role of decomposition methods in applications like land cover classification and intricate scattering analysis. Despite these methods typically requiring fully polarized images, the reconstruction of such images is crucial. Thus, leveraging the aforementioned neural network architecture, we establish a mapping between single-polarized images and the outcomes of Freeman-Durden and H/α^{-}target analysis algorithms. In this paper, the networks are trained using pairs of SAR images, where single-polarization images serve as input and full polarized images act as targets. Subsequently, the trained models are tested on additional SAR images. To illustrate the efficacy of the proposed approach, experiments are conducted using NASA/JPL UAVSAR L-band SAR imagery. Figure (1) displays both single-polarized and fully-polarized images.

a

b

Figure (1). Demonstration of SAR image of the UAVSAR image, a) Single-polarized and b) Full-polarized image

2.1. Freeman Durden Decomposition

This method integrates three fundamental scattering mechanisms (Ballester-Berman, Lopez-Sanchez, & Sensing, 2009; Freeman & Durden, 1998):

- Canopy scatter from randomly oriented dipoles in a cloud-like structure.
- Even- or double-bounce scatter from orthogonal surfaces with distinct dielectric constants.
- Bragg scatter from moderately rough surfaces.

It characterizes the polarimetric scattering of natural objects, distinguishing flooded from non-flooded forests and areas undergoing deforestation or afforestation. Additionally, it calculates scattering mechanisms for VV, HH, and HV polarizations. One fundamental challenge in polarimetric SAR image analysis lies in comprehending the scattering mechanisms linked to the polarization parameters' features. Decomposition methods encounter limitations as they rely solely on mathematical principles, often resulting in combinations of three distribution matrices unrelated to physical distribution models. The standard volume distribution mode matrix S is represented as eq. (1):

$$S = \begin{pmatrix} S_v & 0 \\ 0 & S_h \end{pmatrix} \qquad (1)$$

To derive the scattering matrix for a specific scatterer, it involves transforming to a coordinate system aligned with a standard direction, extracting the field, and subsequently reorienting it to the radar coordinate system. The eq. (2) illustrates the distribution matrix within the radar coordinate system, expressed in terms of the scattering matrix within the distribution coordinate system. The symbol ∅ represents the angle at which the signal impacts the surface.

$$\begin{pmatrix} S_{vv} & S_{vh} \\ S_{hv} & S_{hh} \end{pmatrix} = \begin{pmatrix} \cos\phi & \sin\phi \\ -\sin\phi & \cos\phi \end{pmatrix} S \begin{pmatrix} \cos\phi & -\sin\phi \\ \sin\phi & \cos\phi \end{pmatrix} \qquad (2)$$

And then:

$$\begin{pmatrix} S_{vv} & S_{vh} \\ S_{hv} & S_{hh} \end{pmatrix} = \begin{pmatrix} S_h \sin^2\phi + S_v \cos^2\phi & (S_v - S_h)\cos\phi\sin\phi \\ (S_v - S_h)\cos\phi\sin\phi & S_h \cos^2\phi + S_v \sin^2\phi \end{pmatrix} \quad (3)$$

In this context, it's inferred that S_{hv} is equivalent to S_{vh}, and the coordinate system for both transmitting and receiving radars aligns, resulting in a symmetrical S matrix. The probability density function (PDF) governing the propagation direction conforms to the function f in eq. (4):

$$\langle f \rangle = \int_0^{2\pi} d\phi f(\phi) p(\phi) \quad (4)$$

$$\left\langle |S_{vv}|^2 \right\rangle = a_1 |S_v|^2 + 2a_2 \operatorname{Re}\left|S_h S_v^*\right|^2 + a_3 |S_h|^2$$

$$\left\langle |S_{hh}|^2 \right\rangle = a_1 |S_h|^2 + 2a_2 \operatorname{Re}\left|S_h S_v^*\right|^2 + a_3 |S_v|^2$$

$$\left\langle |S_{hV}|^2 \right\rangle = a_2 |S_V|^2 - 2a_2 \operatorname{Re}\left|S_h S_v^*\right|^2 + a_2 |S_h|^2 \quad (5)$$

$$\left\langle S_{hh} S_{vv}^* \right\rangle = (a_1 + a_3)\operatorname{Re}(S_h S_v^*) + a_2(|S_h|^2 + |S_v|^2)$$
$$+ i(a_1 - a_3)\operatorname{Im}(S_h S_v^*)$$
$$\left\langle S_{hh} S_{hv}^* \right\rangle = a_4(S_h S_v^* - |S_h|^2) + a_5(|S_v|^2 - S_v S_h^*)$$

$$\left\langle S_{hv} S_{vv}^* \right\rangle = a_4(|S_v|^2 - S_h S_v^*) + a_5(S_v S_h^* - |S_h|^2)$$

Where:

$$a_1 \equiv \int_0^{2\pi} d\phi \cos^4\phi p(\phi)$$

$$a_2 \equiv \int_0^{2\pi} d\phi \cos^2\phi \sin^2\phi p(\phi)$$

$$a_3 \equiv \int_0^{2\pi} d\phi \sin^4\phi p(\phi) \quad (6)$$

$$a_4 \equiv \int_0^{2\pi} d\phi \cos^3\phi \sin\phi p(\phi)$$

$$a_5 \equiv \int_0^{2\pi} d\phi \cos\phi \sin^3\phi p(\phi)$$

These relationships can be simplified by assuming a cylindrical distribution. In this scenario, $S_h = 0$ and $S_v = 1$. Thus, we can assume $a_1 = a_3 = \frac{3\pi}{4}$, $a_2 = \frac{\pi}{4}$, and $a_4 = a_5 = 0$. By factoring out π for the volume distribution mode, we obtain eq. (7):

$$\left\langle |S_{hh}|^2 \right\rangle = \left\langle |S_{vv}|^2 \right\rangle = 1$$

$$\left\langle S_{hh} S_{vv}^* \right\rangle = \left\langle |S_{hv}|^2 \right\rangle = \frac{1}{3} \quad (7)$$

$$\left\langle S_{hh} S_{hv}^* \right\rangle = \left\langle S_{hv} S_{vv}^* \right\rangle = 0$$

In double-bounce mode, we model these components using a two-sided surface, each side potentially possessing distinct dielectric properties. Vertical surfaces exhibit reflection coefficients R_{th} and R_{tv} for horizontal and vertical polarizations, respectively. The horizontal surface features Fresnel reflection coefficients R_{gv} and R_{gh}. To account for a broader scenario, we must also incorporate propagation factors $e^{j2\gamma v}$ and $e^{j2\gamma h}$. Here, γ represents a mixed parameter, affecting any attenuation or phase changes of vertically and horizontally polarized waves. This phenomenon occurs during radar transmission to and from the ground, encompassing the effects of diffusion in volume distribution mode. Thus, the matrix S for the Double-bounce distribution is outlined in eq. (8):

$$S = \begin{pmatrix} e^{j2\gamma_v} R_{gv} R_{tv} & 0 \\ 0 & e^{j2\gamma_v} R_{gh} R_{th} \end{pmatrix} \quad (8)$$

In this case, according to the VV term, we will have eq. (9):

$$\left\langle |S_{hh}|^2 \right\rangle = |\alpha|^2$$

$$\left\langle |S_{vv}|^2 \right\rangle = 1$$

$$\left\langle S_{hh} S_{vv}^* \right\rangle = \alpha \quad (9)$$

$$\left\langle \left| S_{hv} \right|^2 \right\rangle = 0$$

$$\left\langle S_{hh} S_{hv}{}^* \right\rangle = \left\langle S_{hv} S_{vv}{}^* \right\rangle = 0$$

Where:

$$\alpha = e^{j^2(\gamma_h - \gamma_v)} \left(\frac{R_{gh} R_{th}}{R_{gv}} R_{tv} \right) \quad (10)$$

Two characteristics of this model in the double-bounce mode are crucial:

- The amplitudes of HH and VV terms must not be equal to each other.
- The phase difference between HH and VV terms should not be equal to ±π.

These features ensure the model closely aligns with the behavior observed in the distribution of natural targets. In this approach, the surface scattering is modeled using a first-order Bragg model. After normalization, the resultant model exhibits as eq. (11):

$$\left\langle \left| S_{hh} \right|^2 \right\rangle = \left| \beta \right|^2$$

$$\left\langle \left| S_{vv} \right|^2 \right\rangle = 1$$

$$\left\langle S_{hh} S_{vv}{}^* \right\rangle = \beta \quad (11)$$

$$\left\langle \left| S_{hv} \right|^2 \right\rangle = 0$$

$$\left\langle S_{hh} S_{hv}{}^* \right\rangle = \left\langle S_{hv} S_{vv}{}^* \right\rangle = 0$$

In this context, it's assumed that β is a real value. Each scattering component assumes mutual scattering, with cross-polarized and co-polarized components considered non-overlapping. Additionally, within this model, the three diffusion mechanisms remain distinct from each other. Consequently, to derive the total surface distribution, the values from these mechanisms are summed together.

$$\left\langle \left| S_{hh} \right|^2 \right\rangle = f_s \left| \beta \right|^2 + f_d \left| \alpha \right|^2 + f_v$$

$$\left\langle \left| S_{vv} \right|^2 \right\rangle = f_s + f_d + f_v$$

$$\left\langle S_{hh} S_{vv}{}^* \right\rangle = f_s \beta + f_d \alpha + f_v / 3 \quad (12)$$

$$\left\langle \left| S_{hv} \right|^2 \right\rangle = f_v / 3$$

$$\left\langle S_{hh} S_{hv}{}^* \right\rangle = \left\langle S_{hv} S_{vv}{}^* \right\rangle = 0$$

If we estimate f_s , f_v and f_d , we can discern the contributions of surface distribution, double-bounce, and volume distribution to HV, HH, and VV distributions. With 4 equations and 5 unknowns (excluding states between Cross-pol and Co-pol), solving for one unknown enables equation resolution. Notably, the HV term isn't linked to the mentioned mechanisms, allowing estimation of volume distribution's share. Removing f_v from the equations leaves us with 4 unknowns and 3 equations:

$$\left\langle \left| S_{hh} \right|^2 \right\rangle = f_s \left| \beta \right|^2 + f_d \left| \alpha \right|^2$$

$$\left\langle \left| S_{vv} \right|^2 \right\rangle = f_s + f_d \quad (13)$$

$$\left\langle S_{hh} S_{vv}{}^* \right\rangle = f_s \beta + f_d \alpha$$

Then, we assess whether the double-bounce or the surface scattering predominantly influence the residuals. If $Re(S_{vv} S_{hh}{}^*)$ is positive, the surface distribution dominates, setting α= -1. Conversely, if this component is negative, the double-bounce distribution prevails, with β=1. Consequently, we derive α, β, f_d and f_s from the remaining radar measurements. This method is most effective when f_d or f_s approach zero, or when α and β equal 1 and -1, respectively. Finally, we evaluate the contribution of each scattering mechanism to the span P. It should be noted that P is only four times the usual expression for total power.

$$P = P_s + P_d + P_v \equiv \left(\left| S_{hh} \right|^2 + 2 \left| S_{hv} \right|^2 + \left| S_{vv} \right|^2 \right) \quad (14)$$

With:

$$P_s = f_s \left(1 + \left| \beta \right|^2 \right)$$

$$P_d = f_d(1+|\alpha|^2) \quad (15)$$

$$P_v = \frac{8f_v}{3}$$

2.2. Eigen-analysis target decomposition

In this approach, we examine the eigenvalues of the Coherency matrix and employ a three-level Bernoulli statistical model to estimate the parameters of the target S matrix (Cloude & Pottier, 1997). The diffusion entropy plays a crucial role in assessing the randomness within this model and serves as a primary parameter in polarimetric challenges encountered in remote sensing. In this approach, we employ a statistical model that presupposes the presence of a consistent distribution mechanism for every pixel, thereby deriving the parameters of this element. Previous research indicates that in environments exhibiting reflection symmetry, the Coherency matrix is approached as follows (Nghiem, Yueh, Kwok, & Li, 1992).

$$\begin{aligned}\langle[T]\rangle &= \frac{1}{2}\left\langle\begin{matrix}(S_{hh}+S_{vv})(S_{hh}+S_{vv})^* & (S_{hh}+S_{vv})(S_{hh}-S_{vv})^* & 2(S_{hh}+S_{vv})S_{hv}^* \\ (S_{hh}-S_{vv})(S_{hh}+S_{vv})^* & (S_{hh}-S_{vv})(S_{hh}-S_{vv})^* & 2(S_{hh}-S_{vv})S_{hv}^* \\ 2S_{hv}(S_{hh}+S_{vv})^* & 2S_{hv}(S_{hh}-S_{vv})^* & 4S_{hv}S_{hv}^*\end{matrix}\right\rangle \\ &= \begin{bmatrix} e^{i\phi}\cos\alpha & e^{i\delta}\sin\alpha & 0 \\ -e^{-i\delta}\sin\alpha & e^{-i\phi}\cos\alpha & 0 \\ 0 & 0 & 1\end{bmatrix}\begin{bmatrix}\lambda_1 & 0 & 0\\ 0 & \lambda_2 & 0\\ 0 & 0 & \lambda_3\end{bmatrix}\begin{bmatrix} e^{-i\phi}\cos\alpha & -e^{-i\delta}\sin\alpha & 0 \\ e^{-i\delta}\sin\alpha & e^{i\phi}\cos\alpha & 0 \\ 0 & 0 & 1\end{bmatrix} \\ &= \begin{bmatrix}\lambda_1\cos^2\alpha+\lambda_2\sin^2\alpha & \cos\alpha\sin\alpha(\lambda_2-\lambda_1)e^{i(\delta+\phi)} & 0\\ \cos\alpha\sin\alpha(\lambda_2-\lambda_1)e^{-i(\delta+\phi)} & \lambda_2\cos^2\alpha+\lambda_1\sin^2\alpha & 0\\ 0 & 0 & \lambda_3\end{bmatrix}\end{aligned} \quad (16)$$

If we assume that λ_2 equals λ_3, this relationship can be expressed as eq. (17):

$$[T] = [U_3]\begin{bmatrix}\lambda_1 & 0 & 0\\ 0 & \lambda_2 & 0\\ 0 & 0 & \lambda_3\end{bmatrix}[U_3]^{*T} \quad (17)$$

Where:

$$[U_3] = \begin{bmatrix}\cos\alpha_1 & \cos\alpha_2 & \cos\alpha_3\\ \sin\alpha_1\cos\beta_1 e^{i\delta_1} & \sin\alpha_2\cos\beta_2 e^{i\delta_2} & \sin\alpha_3\cos\beta_3 e^{i\delta_3}\\ \sin\alpha_1\sin\beta_1 e^{i\gamma_1} & \sin\alpha_2\sin\beta_2 e^{i\gamma_2} & \sin\alpha_3\sin\beta_3 e^{i\gamma_3}\end{bmatrix} \quad (18)$$

This matrix is obtained from the maximum eigenvalues of the matrix [T] and its degree of randomness or entropy is defined through eigenvalues. So we get eq. (19):

$$H = \sum_{i=1}^{n} -P_i \log P_i \qquad P_i = \frac{\lambda_i}{\sum_{i=1}^{n}\lambda_j} \quad (19)$$

In Bragg scattering, entropy (H) is zero, and α depends solely on the incident angle and the dielectric value of the surface, irrespective of surface roughness.

However, this model has two key limitations:

- It's constrained to environments with symmetric reflection, where scattering coefficients in co-pol and cross-pol polarizations don't overlap.
- When λ_2 and λ_3 aren't equal, entropy loses its uniqueness as a measure, leading to polarization dependence on the incident wave's polarization, notably in the presence of spherical diffusers.

2.3. CNN architecture for SAR colorization

U-Net++ or nested U-Net model (Long et al., 2024; Zongwei Zhou, Rahman Siddiquee, Tajbakhsh, & Liang, 2018; Zongwei Zhou, Siddiquee, Tajbakhsh, & Liang, 2019) is designed and developed based on the U-Net model. This model is an advanced architecture in the field of medical image segmentation; In other words, this model is an extension of the original U-Net model, which was proposed

to solve some of the limitations of this model and also to improve its accuracy in the segmentation of medical images. The U-Net++ network consists of an encoder subnet or backbone followed by a decoder subnet.

Unlike U-Net, this model uses redesigned skip paths that connect two subnets and uses deep monitoring (Snoek et al., 2015). In the U-Net model, the feature maps obtained from the encoder network are directly transferred to the decoder network at the same level. But in the U-Net++ model, nested convolutional blocks are used to communicate between encoder and decoder networks, and the number of skip connections between convolutional blocks has increased (Z Zhou, Siddiquee, Tajbakhsh, & Liang). The dense convolutional block makes the feature maps of the encoder network and the corresponding feature maps of the decoder network to be conceptually similar to each other, and the network optimization problem is partially solved and the results are more accurate. U-Net++ is derived from the original U-Net architecture. In a skip path, all convolutional layers are composed of k 3x3 filters. For deep monitoring, each target node is assigned a 1×1 convolution layer with a sigmoid activation function. The final segmentation map is generated by averaging the four segmentation maps generated by U-Net++. Also, in this model, deep monitoring is used to improve the efficiency of the network training process. The architecture of this model is presented in the Figure (2).

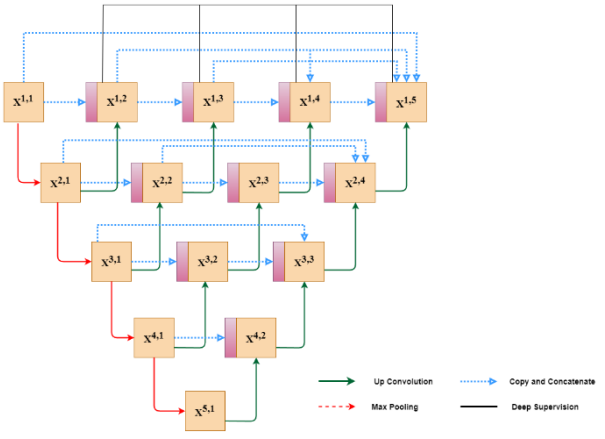

Figure (2). U-Net++ network architecture

The architecture of this network is basically a supervised encoder-decoder deep neural network and similar to U-Net architecture; But in this network, a series of nested and dense skip paths connect the encoder and decoder subnets. Among the innovations in this network is the design of these paths, which is aimed at reducing the semantic gap between the feature maps of encoder-decoder subnets. If the semantic similarity of feature maps of both subnets can be ensured, the optimizer is able to improve the performance of the network in the segmentation process.

The use of nested decoder subnets with dense connections in U-Net++ improves the processing of extracted features and causes better information transfer between encoder-decoder sections. The results of this network are more accurate in image classification compared to the original U-Net model. In other words, with the help of nested connections, this model extracts the features in different depths of the images and improves segmentation accuracy. Also, this will reduce the probability of overfitting the model.

Furthermore, the learning rate, which is an important hyper parameter that impacts the performance of the network during training and convergence, was determined with the aid of the grid search. Several researchers have utilized the torch_lr_finder library, initially developed by Leslie N. Smith (Smith, 2017) for PyTorch, to determine the best learning rate. In order to train the network, this tool gradually increases the learning rate within a specified range.

By analyzing how loss varies with different learning rates, we can pinpoint the optimal rate for training. This is typically observed at the point where the loss function shows a significant decrease, indicating the steepest descent. Initially, the network converges effectively with a low learning rate; however, as the learning rate increases, it may begin to diverge. This iterative approach allows us to discover the ideal learning rate at which the network achieves its best performance (Figure (3)).

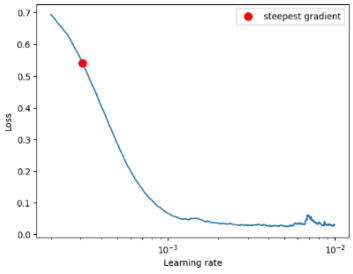

a

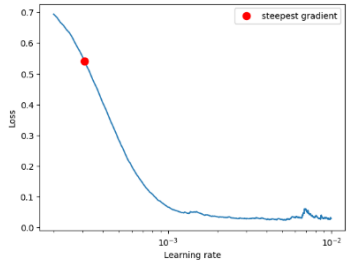

b

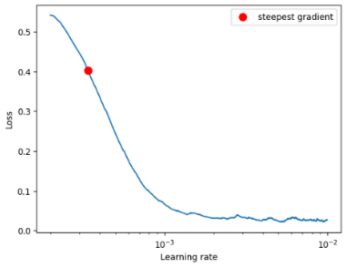

c

Figure (3). Finding learning rate for three networks, a) fully polarized images, b) Freeman-Durden decomposition images, and c) H/α ¯decomposition images Reconstruction.

This model is more complicated than the U-Net, and as a result, a higher computational load and more memory are needed for this model. Also, the increase in the complexity of this model has caused the training time of the model to be relatively longer; Especially when the data set is larger or the resolution of the images is higher. Also, in this model, due to its greater complexity, the hyper parameters must be carefully selected so that the model can perform properly. The general research process is illustrated in Figure (4). As shown, the process begins with the acquisition of the specified dataset. These images are then fed into the UNet++ deep learning model for training. During the training and validation phases, hyper parameters are optimized to fine-tune the model. Once the model is fully trained, it is applied to a set of test images, and its performance is evaluated.

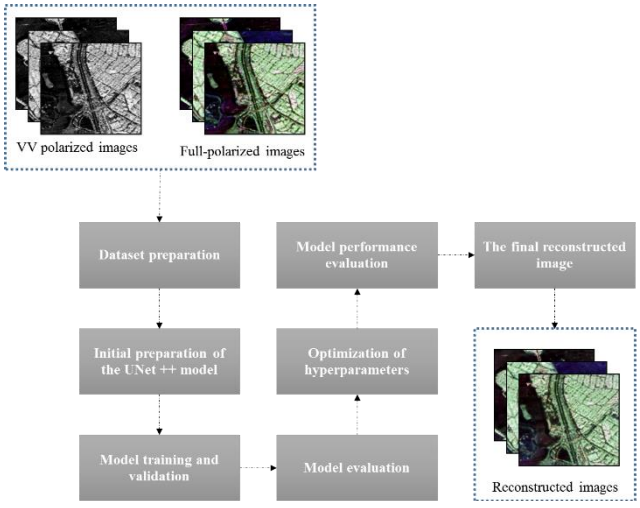

Figure (4). Flowchart of the overall research process

3. Results and Discussion

In order to evaluate the results of this study, a part of the dataset of primary images was selected as test data and then the performance of the model was examined with the help of evaluation criteria such as MAE and MSE between the original fully polarized images and the Reconstructed ones (Chai & Draxler, 2014; Chicco, Warrens, & Jurman, 2021). The equations of these criteria are displayed in eq. (20) and (21). In this equation, y is the actual observed value, p is the estimated value, and n is the number of observations.

$$MSE = \sum \frac{(y_i - p_i)^2}{n} \quad (20)$$

$$MAE = \sum \frac{|y_i - p_i|}{n} \quad (21)$$

In this study, another evaluation criterion was used to analyze results quantitatively. The Universal Image Quality Index, or UIQI (Liu et al., 2023; Wang & Bovik, 2002), evaluates the quality of an image based on its comparison with a reference image. It takes three components into account when comparing the distorted image to the reference image: luminance, contrast, and structure. The UIQI value ranges from -1 to 1, with 1 indicating perfect similarity between images, 0 indicating dissimilarity, and values near -1 suggesting a high level of dissimilarity, possibly accompanied by inversion or severe distortion (eq. (22)).

$$UIQI = \frac{4\sigma_{xy}\mu_x\mu_y}{(\sigma_x^2 + \sigma_y^2)(\mu_x^2 + \mu_y^2)} \quad (22)$$

μ_x and $\mu_y$represent the original image and the distorted image, respectively. σ_x^2 and σ_y^2 are the variances between the original and distorted images. In this case, σ_{xy} is the covariance between the original image and the distorted image. Figure (5) shows the process of MSE loss changes during the process of training single polarized images and converting them to fully polarized images. Moreover, this image illustrates the process of changes of this function during the training of two other networks in order to reconstruct Freeman-Durden and H/α decompositions from single polarized images. All three networks (as illustrated in this figure) showed a completely downward trend in MSE values during the training process. This indicates that all three networks are convergent.

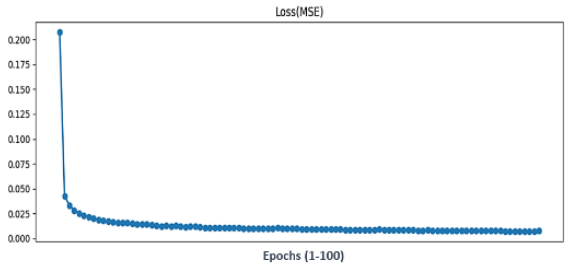

a

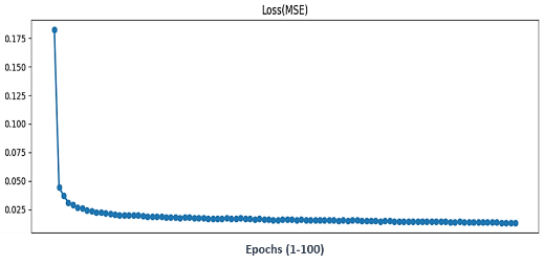

b

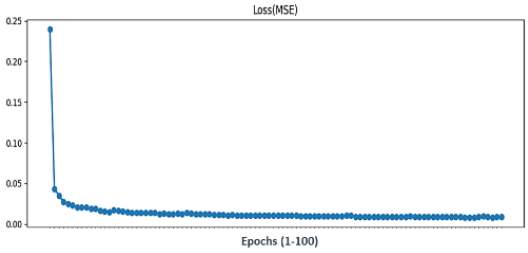

c

Figure (5). The trend of changes in the MSE criterion, a) Reconstruction of fully polarized images, b) Reconstruction of Freeman-Durden decomposition images, and c) Reconstruction of H/$\alpha\bar{}$ decomposition images

The following table shows the values of MSE, MAE and UIQI for three processes of converting single polarized images into fully polarized images, the results of Freeman-Durden and H/α decomposition algorithms. The deep learning model demonstrates successful execution of the image reconstruction process, as indicated by the results in Table (1). As shown, the MAE values for these three methods are below 0.1. According to the study (Song, Xu, & Jin, 2018; Q. Song, F. Xu, & Y.-Q. J. I. A. Jin, 2017), this suggests that the deep learning models perform well in the image reconstruction process. In the reconstruction process of fully polarized images and H/α decomposition images, the MAE value has been equalled and is lower than the MAE value in the Freeman-Durden decomposition reconstruction, indicating a higher degree of accuracy with these two methods. It is also true for the MSE values, which generally fall below 0.025 for all three trends. Additionally, the UIQI values, which reflect the degree of similarity between the reconstructed images and the original, are generally above 90%, indicating that the images are at least 90% similar. Specifically, the UIQI values for the reconstruction of fully polarized images surpass those of the other two processes, reaching 95.95%. This demonstrates the excellent performance of the deep learning model in reconstructing fully polarized images.

Table (1). Model evaluation criteria in three different processes

The type of reconstructed images	MAE	MSE	UIQI(%)
Full pol	0.063	0.010	95.95
Freeman-Durden	0.087	0.022	90.35
H/$\alpha\bar{}$	0.063	0.010	95.83

One of the objectives of this research is to reconstruct fully polarimetric images from single-polarized VV images. The results are presented in Figure 6. In the first row (a) of this figure, the original single-polarized VV images are displayed. The corresponding fully polarimetric images are shown in the second row (b). The third row (c) illustrates the reconstructed fully polarimetric images generated by our method. Finally, the fourth row (d) highlights the differences between the original and reconstructed fully polarimetric images. As illustrated in the Figure (6), the reconstruction of the fully polarized images stands out compared to the results from the other two methods. The reconstructed images closely resemble the original images, with minimal differences between them. This suggests that image reconstruction utilizing deep learning models are highly effective, which are often inaccessible in many areas.

a

b

c

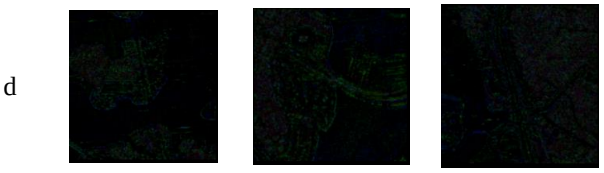

Figure (6). Reconstruction of fully polarized images from single polarized images, a) single polarized images (VV), b) full-pol images, c) reconstructed images by model, d) difference of original images and reconstructed images.

In interpreting various objects in radar images, fully polarized images are crucial, but different decompositions, often derived from these fully polarized images, also play a significant role. Each decomposition technique excels in interpreting specific types of objects, and the choice of decomposition depends on the surface characteristics being analysed. For this study, we focused on two decompositions, H/α and Freeman-Durden, as they have demonstrated superior performance in analysing three main land cover classes: vegetation, residential areas, and water bodies. The visual results demonstrate that the UNet++ deep learning model has performed exceptionally well in reconstructing images from these two decompositions. A comparison between the reconstructed and original images, along with an analysis of their differences, reveals a high degree of similarity, highlighting the model's effectiveness.

Figure (7) presents the results of this method in reconstructing decomposition features. The first row (a) displays the single-polarized VV images used as input data. The second row (b) shows the original Freeman-Durden feature decomposition images, while the third row (c) depicts the reconstructed images. The differences between the original and reconstructed images are highlighted in the fourth row (d).

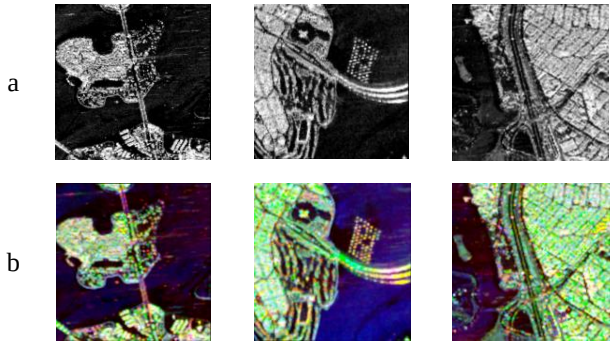

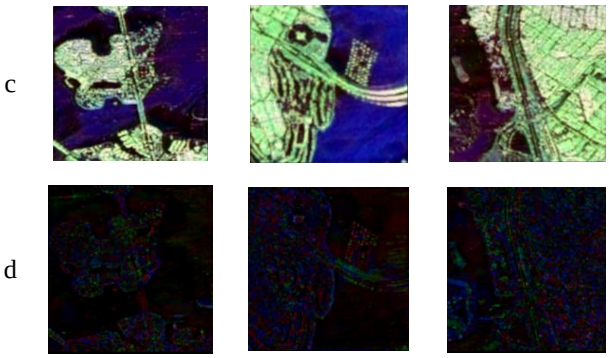

Figure (7). Reconstruction of Freeman-Durden decomposition images from single polarized images, a) single polarized images (VV), b) output of Freeman-Durden decomposition, c) reconstructed images by model, d) difference of original images and reconstructed images.

Figure 8 displays the results of image reconstruction for H/α feature decomposition. The first row (a) shows the monopolarized VV images. The second row (b) presents the original H/α decomposition feature images, while the third row (c) contains the reconstructed images. The fourth row (d) highlights the differences between the original and reconstructed images.

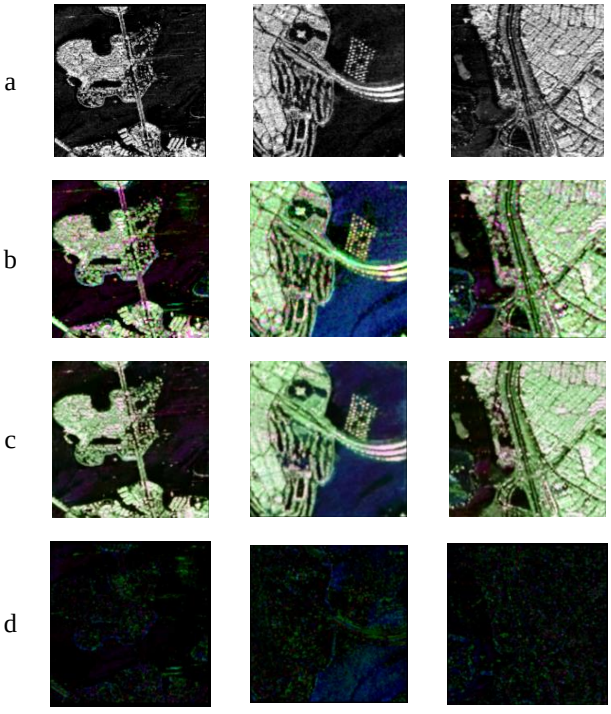

Figure (8). Reconstruction of H/α ¯decomposition images from single polarized images, a) single polarized images (VV), b) output of H/α ¯decomposition, c) reconstructed

images by model, d) difference of original images and reconstructed images.

The results obtained in this study demonstrate the efficacy of deep learning models, such as UNet++, in reconstructing fully polarized images or the results derived from decomposition algorithms applied to them. This capability is particularly significant as it provides a viable method for generating fully polarized images from single-polarized ones, which addresses the challenge posed by the limited availability of fully polarized images. Fully polarized images are crucial for in-depth analysis and interpretation of terrestrial features, yet they are often less available than single-polarized images due to various constraints, including acquisition difficulties and the higher complexity of the imaging process. By utilizing deep learning models to reconstruct these images, this research offers a solution to bridge the gap caused by the scarcity of fully polarized images.

The ability to reconstruct fully polarized images enhances our understanding and interpretation of various terrestrial phenomena. This advancement not only facilitates more accurate and comprehensive analyses but also supports more effective monitoring and assessment of environmental and land cover changes. As fully polarized images become increasingly accessible through these reconstruction techniques, their importance in providing detailed and nuanced insights into the Earth's surface is further underscored.

4. Conclusion

In this study, we effectively demonstrated the potential of deep learning techniques, specifically the UNet++ architecture, to convert single-polarized SAR images into fully polarized ones. This conversion is essential for applications that require fully polarized data but face limitations due to the scarcity of such data in various geographical regions. For training and testing, we utilized the NASA/JPL UAVSAR L-band SAR images, a robust and reliable dataset.

The results of our experiments revealed that the deep learning models, including the UNet++ model, were highly effective in reconstructing fully polarized SAR images with remarkable accuracy. The MAE and MSE values for the reconstructed images were consistently below 0.1, demonstrating the models' ability to minimize errors during the reconstruction process. Additionally, UIQI scores were close to 1, further confirming the high quality of the reconstructed images compared to the original fully polarized images.

We also extended our approach to the reconstruction of PolSAR target decomposition images, specifically the Freeman-Durden and H/α decompositions. The models achieved similar levels of accuracy, with MAE and MSE values again below 0.1, and UIQI scores reflecting a strong similarity between the reconstructed and original decomposition images. Notably, the model exhibited higher accuracy in reconstructing fully polarized and H/α decomposition images compared to the Freeman-Durden decomposition, indicating its robustness in handling different types of PolSAR data.

In conclusion, the deep learning framework we proposed not only improves access to fully polarized SAR data by converting single-polarized images but also provides a reliable method for reconstructing PolSAR target decomposition features. This study lays a solid foundation for further research into applying similar techniques to other types of SAR data and decomposition features, thereby expanding the potential applications of SAR technology in remote sensing and earth observation.

Reference

Ballester-Berman, J. D., Lopez-Sanchez, J. M. J. I. T. o. G., & Sensing, R. (2009). Applying the Freeman–Durden decomposition concept to polarimetric SAR interferometry. 48(1), 466-479. (https://doi.org/ 10.1109/TGRS.2009.2024304)

Chai, T., & Draxler, R. R. (2014). Root mean square error (RMSE) or mean absolute error (MAE)?–Arguments against avoiding RMSE in the literature. *Geoscientific model development*, *7*(3), 1247-1250. (https://doi.org/10.5194/gmd-7-1247-2014, 2014)

Chan, Y. K., & Koo, V. (2008). An introduction to synthetic aperture radar (SAR). *Progress In Electromagnetics Research B*, *2*, 27-60. (https://doi.org/10.2528/PIERB07110101)

Chicco, D., Warrens, M. J., & Jurman, G. (2021). The coefficient of determination R-squared is more informative than SMAPE, MAE, MAPE, MSE and RMSE in regression analysis evaluation. *PeerJ Computer Science*, *7*, e623. (https://doi.org/10.7717/peerj-cs.623)

Cloude, S. R., & Pottier, E. (1997). An entropy based classification scheme for land applications of polarimetric SAR. *IEEE transactions on Geoscience and Remote Sensing*, *35*(1), 68-78. (https://doi.org/10.1109/36.551935)

Freeman, A., & Durden, S. L. (1998). A three-component scattering model for polarimetric SAR data. *IEEE transactions on Geoscience and Remote Sensing*, *36*(3), 963-973. (https://doi.org/10.1109/36.673687)

Levin, A., Lischinski, D., & Weiss, Y. (2004). Colorization using optimization. In *ACM SIGGRAPH 2004 Papers* (pp. 689-694).

(https://doi.org/10.1145/1186562.101578)

Liu, Y., Gu, K., Cao, J., Wang, S., Zhai, G., Dong, J., & Kwong, S. J. I. T. o. M. (2023). UIQI: A comprehensive quality evaluation index for underwater images. (https://doi.org/10.1109/TMM.2023.3301226)

Long, C., Tan, C., Li, Q., Tan, H., Duan, L. J. N. T., & Evaluation. (2024). Industrial CT image reconstruction for faster scanning through U-Net++ with hybrid attention and loss function. 1-20.(https://doi.org/10.1080/10589759.2024.2305329)

Nghiem, S., Yueh, S., Kwok, R., & Li, F. (1992). Symmetry properties in polarimetric remote sensing. Radio Science, *27*(05), 693-711. (https://doi.org/10.1029/92RS01230)

Oveis, A. H., Giusti, E., Ghio, S., Martorella, M. J. I. A., & Magazine, E. S. (2021). A survey on the applications of convolutional neural networks for synthetic aperture radar: Recent advances. *37*(5), 18-42. (https://doi.org/10.1109/MAES.2021.3117369)

Shirvany, R., Chabert, M., & Tourneret, J.-Y. (2012). Estimation of the degree of polarization for hybrid/compact and linear dual-pol SAR intensity images: Principles and applications. *IEEE transactions on Geoscience and Remote Sensing, 51*(1), 539-551. (https://doi.org/10.1109/TGRS.2012.2202242)

Smith, L. N. (2017). *Cyclical learning rates for training neural networks.* Paper presented at the 2017 IEEE winter conference on applications of computer vision (WACV). (https://doi.org/10.1109/WACV.2017.58)

Snoek, J., Rippel, O., Swersky, K., Kiros, R., Satish, N., Sundaram, N., . . . Adams, R. (2015). *Scalable bayesian optimization using deep neural networks.* Paper presented at the International conference on machine learning.

Song, Q., Xu, F., & Jin, Y.-Q. (2017). Radar image colorization: Converting single-polarization to fully polarimetric using deep neural networks. *IEEE Access, 6*, 1647-1661. (https://doi.org/10.1109/ACCESS.2017.2779875)

Song, Q., Xu, F., & Jin, Y.-Q. (2018). *Reconstruction of full-pol SAR data from partialpol data using deep neural networks.* Paper presented at the IGARSS 2018-2018 IEEE International Geoscience and Remote Sensing Symposium. (https://doi.org/10.1109/IGARSS.2018.8518094)

Wang, Z., & Bovik, A. C. J. I. s. p. l. (2002). A universal image quality index. *9*(3), 81-84. (https://doi.org/10.1109/97.995823)

Zhang, Z., Wang, H., Xu, F., & Jin, Y.-Q. (2017). Complex-valued convolutional neural network and its application in polarimetric SAR image classification. *IEEE transactions on Geoscience and Remote Sensing, 55*(12), 7177-7188. (https://doi.org/10.1109/TGRS.2017.2743222)

Zhou, Y., Wang, H., Xu, F., & Jin, Y.-Q. (2016). Polarimetric SAR image classification using deep convolutional neural networks. *IEEE Geoscience and Remote Sensing Letters, 13*(12), 1935-1939. (https://doi.org/10.1109/LGRS.2016.2618840)

Zhou, Z., Rahman Siddiquee, M. M., Tajbakhsh, N., & Liang, J. (2018). *Unet++: A nested u-net architecture for medical image segmentation.* Paper presented at the Deep Learning in Medical Image Analysis and Multimodal Learning for Clinical Decision Support: 4th International Workshop, DLMIA 2018, and 8th International Workshop, ML-CDS 2018, Held in Conjunction with MICCAI 2018, Granada, Spain, September 20, 2018, Proceedings 4. (https://doi.org/10.1007/978-3-030-00889-5_1)

Zhou, Z., Siddiquee, M. M. R., Tajbakhsh, N., & Liang, J. (2019). Unet++: Redesigning skip connections to exploit multiscale features in image segmentation. *IEEE transactions on medical imaging, 39*(6), 1856-1867. (https://doi.org/10.1109/TMI.2019.2959609)